applied sciences

MDPI

Article

Measurement and Analysis of Channel Characteristics in Reflective Environments at 3.6 GHz and 14.6 GHz

Xin Zhou [1,2], Zhangdui Zhong [1], Xin Bian [2], Ruisi He [1,*], Ruoyu Sun [3], Ke Guan [1], Ke Liu [2] and Xiaotao Guo [2]

1 State Key Laboratory of Rail Traffic Control and Safety, Beijing Jiaotong University, Beijing 100044, China; zhouxin@nim.ac.cn (X.Z.); zhdzhong@bjtu.edu.cn (Z.Z.); kguan@bjtu.edu.cn (K.G.)
2 Division of Electronics and Information Technology, National Institute of Metrology, Beijing 100013, China; bianx@nim.ac.cn (X.B.); liuke@nim.ac.cn (K.L.); guoxiaotao@nim.ac.cn (X.G.)
3 Communications Technology Laboratory, National Institute of Standards and Technology, Boulder, CO 80303, USA; ruoyusun@ieee.org
* Correspondence: ruisi.he@bjtu.edu.cn; Tel.: +86-10-5168-4773

Academic Editor: Dimitrios G. Aggelis
Received: 18 November 2016; Accepted: 3 February 2017; Published: 13 February 2017

Abstract: Recently, high frequency bands (above 6 GHz) have attracted more attention for the next generation communication systems due to the limited frequency resources below 6 GHz. To reveal the influence of frequency on propagation channels, channel characterization results at 14.6 and 3.6 GHz bands based on measurements in an indoor scenario and in a reverberation chamber are presented. The measurement results indicate minimal differences in path loss exponents, shadow fading standard deviation, root-mean-square (RMS) delay spread and coherence bandwidth for the two frequency bands, while the path loss at 14.6 GHz band is clearly larger than that at the 3.6 GHz band. Furthermore, the underlying factors that influence the channel characteristics are investigated. It is found that the RMS delay spread is independent of the frequency in the scenario where free space propagation and/or reflection are the main mechanisms. Measurements in the reverberation chamber verify this inference.

Keywords: propagation measurement; comparative analysis; indoor scenario; wideband characteristics; reverberation chamber

1. Introduction

Achieving a high data rate is one of the key challenges for the next-generation wireless communication systems. Hence, large frequency bandwidth is required. Such large bandwidth cannot be achieved on radio links operating at low frequency bands (below 6 GHz). Therefore, high frequency bands (above 6 GHz) have been widely considered for future applications [1]. It is well known that the design of a wireless system requires a deep understanding of the propagation channels. However, most available channel models, e.g., WINNER II/+ and International Mobile Telecommunications-Advanced models, have been designed for the frequency range below 6 GHz. Thus, Mobile and wireless communications Enablers for the Twenty-twenty Information Society (METIS) indicates that measurement data above 6 GHz is crucial for the needed extensions/modifications of available channel modeling [2]. In this paper, measurement-based characterization for the corridor scenario at 14.6 GHz is presented. To reveal the influence of frequency on the channel characteristics, characterization for the same scenario at 3.6 GHz is also presented.

As one of the candidate frequency bands for the fifth generation (5G) system, the 14 GHz band has more than 0.7 GHz bandwidth (14.3–15 GHz) to be allocated [3]. Some 5G tests using this frequency

band demonstrate data rates up to 4.5 Gbps [4]. The 3.6 GHz band is also suitable for providing capacity to fulfill the increasing traffic requirements, especially for small coverage with denser network deployment [3].

Stochastic channel models reproduce the statistics of the channel parameters based on the realistic measurements and have been widely used [5–7]. Based on measurements, several papers have provided comparisons between some different frequency bands [8–10]. In [8], a multi-frequency outdoor-to-indoor path loss model for different frequency bands ranging from 0.8 GHz to 28 GHz was presented. In [9], the path loss and wideband characteristics were measured at 1.7 GHz and 60 GHz for small cell systems. Omnidirectional and directional antennas were used for 1.7 GHz and 60 GHz, respectively. The difference between the antennas limited the effectiveness of the comparison. In [10], measured data and empirical models for 2–10 GHz and 57–66 GHz were presented. In this work, the measurements were performed in a laboratory and the distance between the transmitter and receiver was less than 4 m. The scenario is different from our work and leads to different results on the frequency dependency for some channel characteristics (for details, see the Comparative Analysis section).

This paper focuses on the reflective environments where free space propagation and/or reflection are the main mechanisms. A comparative analysis of the channel characteristics between the low and high frequency bands is presented. The main contributions of our work are summarized as follows:

- A detailed insight into the channel characteristics of the path loss, RMS (root-mean-square) delay spread and coherence bandwidth in the corridor scenario with the directional antennas at 3.6 GHz and 14.6 GHz frequency bands is presented.
- A comparative analysis is made for statistical metrics of the propagation channel between the two frequency bands.
- The underlying factors that lead to the influence of frequency on the channel characteristics are investigated. It is found that, in the corridor, the differences between the two frequency bands in RMS delay spread are minimal (less than 1 ns). Measurements in the reverberation chamber (RC) verify this inference.

The remainder of this paper is organized as follows: Section 2 describes our measurement system and measurement scenario. Section 3 presents the measurement results. Section 4 focuses on the comparative analysis. In Section 5, some auxiliary experiments in an RC are described to support the analysis. Section 6 concludes this paper.

2. Measurements

2.1. Measurement System

The wideband frequency responses of the propagation channel were measured with a measurement system based on a vector network analyzer (VNA) (MS2038C, Anritsu, Morgan Hill, CA, USA). The scattering parameter S_{21} was measured over a 0.8 GHz bandwidth and centered at 3.6 GHz and 14.6 GHz, respectively. The VNA was set to transmit 1024 continuous wave tones uniformly distributed over each frequency band, which results in a frequency step of about 0.78 MHz. The frequency resolution further yields a maximum excess delay of 1280 ns, i.e., a maximum distance range of approximately 384 m. Intermediate-frequency (IF) averaging bandwidth was set to 300 Hz. To reduce noise, six sweeps were averaged.

The antennas used in measurements are directional horn antennas. Radiation patterns of antennas were measured in an anechoic chamber in the National Institute of Metrology, Beijing, China and are given in Figure 1 and Table 1. Although the beamwidths of the two frequency bands are not exactly the same, given the fact that the corridor is a very narrow and closed space, the angles of departure and angles of arrival for all major multipath components are expected inside the main beamwidth at both frequencies, which means that the difference of the beamwidths will not effectively influence the channel properties at the two frequencies under study. The use of the directional antennas is common

at the high frequency band, e.g., [11,12]. The antennas were mounted on wooden tripods with a small section of metal behind the directional antennas, which does not influence the pattern.

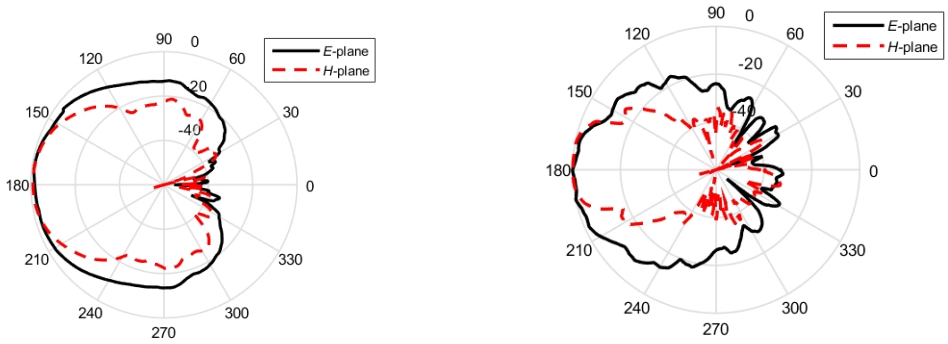

(a) (b)

Figure 1. (color online) Radiation patterns of antennas at (**a**) 3.6 GHz; and (**b**) 14.6 GHz.

Calibration was performed in an anechoic chamber to compensate the frequency response of antennas and cables as suggested in [13]. These two measured bands were free from interference during the measurement campaign, as confirmed by measurements with a spectrum analyzer (PSA E4445A, Agilent, Santa Clara, CA, USA). A summary of the measurement parameters is listed in Table 1.

It is worth noting that the channel characteristics are extremely sensitive to antenna placements [14]. To extract the influence of frequency on the channel characteristics, the measurements for the two frequency bands should be carried out at the exact same antenna placement and in the exact same scenario. To this end, the measurement process is designed as follows. Firstly, the VNA is calibrated by using a “response" calibration [12]. The calibration is carried out for the two frequency bands, respectively. In addition, the calibration data for the two frequency bands are stored in the internal memory of the VNA. For each measurement position, calibration data for 3.6 GHz band is recalled and the measurement for 3.6 GHz band is executed. Then, immediately, without the antennas moved, calibration data for 14.6 GHz band is recalled and the measurement for 14.6 GHz band is executed. In this way, the measurements for the two frequency bands are carried out at the exact same antenna placement, in the exact same scenario, and almost at the exact same time. This design effectively reduces the uncertainty in the comparative analysis of channel characteristics between the two frequency bands.

Table 1. Measurement parameters.

Parameter	Value	
Center Frequency	3.6 GHz	14.6 GHz
Beamwidth *E*-plane	49°	43°
Beamwidth *H*-plane	38°	34°
Gain *E*-plane	7 dBi	12 dBi
Gain *H*-plane	9 dBi	14 dBi
Sweep Bandwidth	0.8 GHz	
Time Resolution	1.25 ns	
IF Bandwidth	300 Hz	
Acquistion Time (6 sweeps× 900 ms)	5.4 s	

2.2. Measurement Scenario

The measurements have been carried out in the second-floor corridor in the 18th building, National Institute of Metrology, Beijing, China. The building is constructed of concrete with faculty

offices and laboratories as shown in Figure 2. The corridor is 20 m in length, 2.4 m in width and 2.8 m in height. The side walls, floor and ceiling of the corridor are constructed of concrete. The floor is covered with ceramic tiles and the ceiling is covered with polystyrene tiles. The corridor has a number of wooden doors and some windows. In the measurements, the doors and the windows were closed and no people were moving around.

Figure 2. Measurement environment.

The transmitter (TX) is fixed and denoted by the solid star in Figure 3 (top view). At the receiver side (RX), the antenna is moved along a straight line at 17 different locations, which are denoted as the solid circles in Figure 3. The TX and RX are placed in the middle of the corridor (the distances to both sides of the corridor are 1.2 m). The distance between the TX and RX (1) is 1.2 m. The distances between two adjacent RX locations are also 1.2 m. The transmitted and received antennas are vertically polarized in the elevation plane and fixed on adjustable tripods about 1.4 m above the ground. The height of the antenna was set to simulate the communication between two portable devices, and it will not vary much for most personal applications.

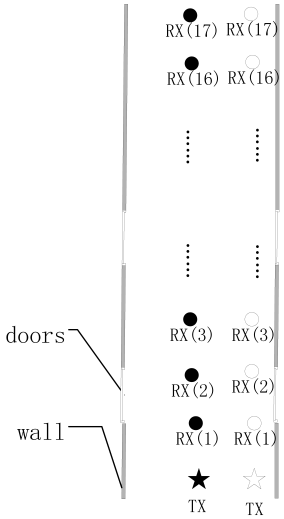

Figure 3. Floor plan.

In order to analyze the influence of antenna location (whether near the walls) on channel characteristics, we conducted another measurement in the same scenario. All the measurement settings were the same as the previous measurements, but the TX and RX antennas were placed 0.5 m from the wall. As shown in Figure 3, the TX and RX are denoted by the hollow star and hollow circles, respectively.

In order to achieve spatial averaging, five spatially separated positions were measured at each receiver location as suggested in [15]. One received position is at the center of one specific location, surrounded by the remaining four positions as shown in Figure 4 (top view); these positions are separated by about 0.17 m, which is about two wavelengths for 3.6 GHz and eight wavelengths for 14.6 GHz. Assuming that the phase of received signal is uniformly distributed, it is reasonable to average out the small-scale fading effect via these five positions [15] in the Ricean channel.

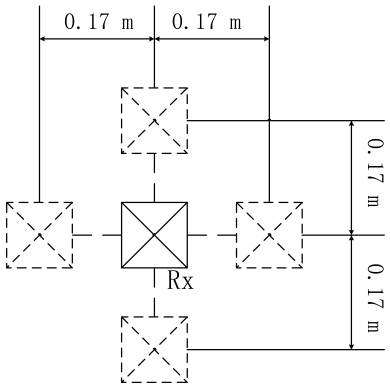

Figure 4. Positions of RX (receiver side) at each location.

3. Parameter Extraction and Measurement Results

3.1. Path Loss Exponent and Shadow Fading

In the widely accepted power-law path loss model, the change of the path loss along with the TX–RX distance is depicted by the path loss exponent. Such exponent and shadow fading are extracted from the measured results by using the following expression:

$$PL(d) = PL(d_0) + 10nlog_{10}(d/d_0) + X, \quad (1)$$

where d is the distance between the TX and RX, and $PL(d)$ is the path loss (small-scale fading has already been filtered out) at d. d_0 denotes the reference distance and n is the path loss exponent. X is the shadow fading, which is well fitted by the log-normal distribution by passing Kolmogorov–Smirnov, Anderson–Darling, and chi-squared tests [16]. By using the least-square criterion, the path loss exponent n can be obtained.

3.2. Delay Spread

The RMS delay spread is widely used to characterize the delay dispersion of the channel. By taking the inverse Fourier transform of the measured transfer function, the power delay profile (PDP) and RMS delay spread of the channel are obtained. The RMS delay spread is defined as the second moment of the PDP [17] and expressed as

$$\tau_{RMS}(d) = \sqrt{\frac{\sum_i PDP(d,\tau_i)\tau_i^2}{\sum_i PDP(d,\tau_i)} - (\frac{\sum_i PDP(d,\tau_i)\tau_i}{\sum_i PDP(d,\tau_i)})^2}, \quad (2)$$

where τ_i and $PDP(d,\tau_i)$ represent the delay and corresponding delay power of the i_{th} mutipath component (MPC) measured at the distance of d, respectively. When computing the RMS delay spread, we set the power of all the MPCs below a threshold to zero to reduce the impact of the noise. The threshold is set to be 6 dB above the noise floor [18].

3.3. Coherence Bandwidth

The coherence bandwidth is a statistical measure of the range of frequencies over which two frequency components have a strong potential for amplitude correlation. The coherence bandwidth B_ρ is calculated as [19]

$$B_\rho = \frac{1}{2}[\underset{\delta f>0}{arg\ max}(\frac{|R_H(0,\delta f)|}{R_H(0,0)} = \rho) - \underset{\delta f<0}{arg\ min}(\frac{|R_H(0,\delta f)|}{R_H(0,0)} = \rho)], \quad (3)$$

where R_H is the frequency correlation function, δf is frequency separation, and ρ is the correlation level.

3.4. Measurement Results

Table 2 shows the measured channel characterization results for the two frequency bands with the directional antennas in the corridor scenario. The following findings can be summarized: (1) the differences in the path loss exponent, shadow fading standard deviation, RMS delay spread and coherence bandwidth for the two frequency bands are minimal; (2) the path loss at 14.6 GHz is larger than that at 3.6 GHz. As expected, the difference is about $20log_{10}$(14.6 GHz/3.6 GHz) = 12.16 dB between the two carrier frequencies; and (3) there is no significant difference in all of the extracted propagation characteristics between different antenna locations (near the wall or in the middle of the corridor).

Table 2. Measurement results at the two frequency bands.

Measured Parameters	3.6 GHz Band		14.6 GHz Band	
	In the Middle	Near the Wall	In the Middle	Near the Wall
Path Loss Exponent	1.51	1.69	1.67	1.58
Fit Intercept (dB)	47.8	46.8	57.8	58.9
Shadow Fading Standard (dB)	1.79	2.19	2.27	2.16
Mean of RMS Delay Spread (ns)	12.94	13.04	14.84	13.87
$B_{0.5}$ (MHz)	324.95	316.19	322.27	324.56
$B_{0.7}$ (MHz)	115.92	126.29	117.42	122.60
$B_{0.9}$ (MHz)	37.21	42.91	43.15	42.17
$B_{0.5,min}$ (MHz)	11.01	11.22	12.05	11.70
$B_{0.7,min}$ (MHz)	5.21	6.07	5.16	5.78
$B_{0.9,min}$ (MHz)	1.52	1.62	1.77	1.40

The path loss exponent in the corridor ranges from 1.51 to 1.69 (see Table 2), smaller than two (which corresponds to the free-space propagation). This implies a waveguide phenomenon due to the confined structure of the corridor. In addition, the minimal difference between different antenna locations (near the wall or in the middle) implies that the wave-guide effect is not very sensitive to the antenna–wall distance in the corridor scenario with the directional antennas. The standard deviation of shadow fading ranges from 1.79 to 2.27 dB, which agrees with those measurements in corridors at 2.4 GHz, 5.3 GHz, and 60 GHz [20–22].

No single definitive value of correlation has emerged for the specification of coherence bandwidth. Hence, coherence bandwidths for generally accepted values of correlations coefficient equal to 0.5, 0.7 and 0.9 are evaluated, and these are referred to as $B_{0.5}$, $B_{0.7}$ and $B_{0.9}$. Furthermore, the coherence bandwidth is highly variable with the locations of receiver. By convention, cumulative distribution function (CDF) of the coherence bandwidth is computed and the level below which the coherence bandwidth stays for a given percentage is used to interpret the coherence bandwidth results [13]. As shown in Table 2, the level of $B_{0.5}$, $B_{0.7}$ and $B_{0.9}$ for 90% of receiver positions is about 320 MHz, 120 MHz and 40 MHz, respectively. The communication system designers sometimes rely on the lowest value of the coherence bandwidth. Thus, the lowest value, $B_{\rho,min}$, is also listed in Table 2.

4. Comparative Analysis

4.1. Example APDPs

We denote the PDP averaged over the five spatial points (see Figure 4) as the averaged PDP (APDP) [23]. In Figure 5, we observe the APDPs for both frequency bands. For the example APDPs, the TX and RX are placed in the middle of the corridor and the TX–RX distance is 1.2 m. For visual comparison, we have normalized the line-of-sight (LOS) contribution to 0 dB.

It is observed that the main components fit the same delays. For both frequency bands, the delay of the largest component is about 4 ns, which, multiplied by the velocity of light, equals the LOS distance (1.2 m).

Figure 5 clearly illustrates multipath propagation. From basic trigonometry, the excess distances (compared with the LOS path) for the ground reflected path, the ceiling reflected path and the wall reflected paths are 1.85 m, 1.85 m, 1.43 m and 1.43 m, respectively. The distance differences divided by the velocity of light are from 4.77 and 6.16 ns. The components (area highlighted by red box in Figure 5) are likely the combination of all the four reflected paths since the relative excess delay is also between 4.77 and 6.16 ns.

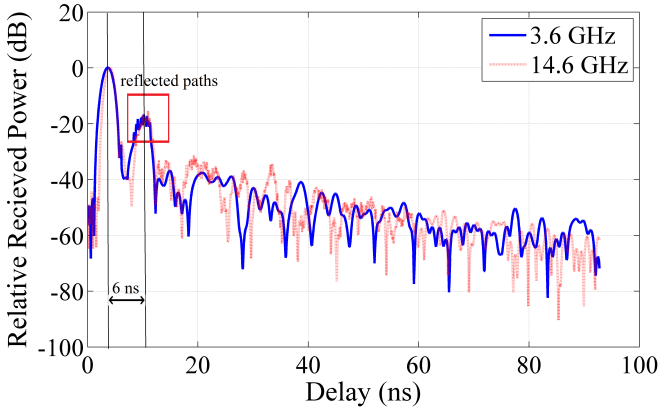

Figure 5. (color online) Normalized APDPs (averaged power delay profile) at 3.6 GHz and 14.6 GHz.

Figure 5 also indicates that the normalized amplitudes of the reflected paths are similar for the two bands. The received power for the LOS component at RX is

$$P_{RX,LOS} = \frac{P_t G_t}{4\pi d_{LOS}^2} A_e, \tag{4}$$

where P_t is the transmitted power, G_t is the transmitter antenna gain, A_e is the RX antenna effective area, and d_{LOS} is the distance for the LOS path as shown in Figure 6. For a reflected component, the received power at the RX is [24]

$$P_{RX,r} = \frac{P_t G_t |\Gamma|^2}{4\pi (d_{r1} + d_{r2})^2} A_e, \tag{5}$$

where (Γ) is the reflection coefficient, d_{r1} is the distance between the TX and the reflecting point, and d_{r2} is the distance between the RX and the reflecting point. The power ratio between the LOS component and reflected component is

$$\frac{P_{RX,r}}{P_{RX,LOS}} = \frac{|\Gamma|^2 d_{LOS}^2}{(d_{r1} + d_{r2})^2}. \tag{6}$$

The reflection coefficient (Γ) is determined by the complex dielectric constant, δ, and δ is defined as [19]

$$\delta = \epsilon - j\frac{\sigma_e}{2\pi f}, \tag{7}$$

where j is the imaginary unit, ϵ is the dielectric constant, and σ_e is the conductivity. As σ_e is very small [25], the imaginary part in Equation (7) becomes negligible. In addition, ϵ stays constant with a large frequency range (1–100 GHz) for many typical building materials (e.g., concrete, wood, glass and chipboard) [25]. Thus, the reflection coefficient is almost independent of the frequency. Then, via Equation (6), the power ratio between the LOS component and reflected component (i.e., the normalized power for the reflected path) is almost independent of the frequency.

The similar delays and normalized amplitudes should yield similar RMS delay spread.

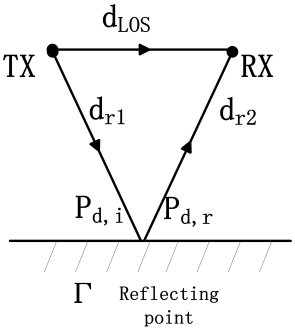

Figure 6. Illustration of the LOS (line-of-sight) path and a reflected path.

4.2. RMS Delay Spread

Table 2 indicates a minimal difference in the RMS delay spread for the two frequency bands. The statistical results are consistent with the above theoretical prediction. This phenomena has also been observed in the measurements of [26,27], where the RMS delay spreads from 2.4 GHz to 28 GHz are similar for the indoor LOS and non-LOS (NLOS) channels. However, some papers present different results. For example, in [10], for LOS, the RMS delay spread is around 8 and 4 ns for 2–10 and 57–66 GHz, respectively. The measurements were performed in a laboratory furnished with several closets, shelves, desk, and chairs. In this scenario, there are not only free space propagation and reflection but also the diffraction. The diffraction gain is frequency-dependent [24]. This may be the reason for the difference of the RMS delay spread in this scenario.

Because the reflection coefficient is insensitive to the frequency with the large frequency range for many typical building materials, it is reasonable to hypothesize that the RMS delay spread is also independent of the frequency in the scenario with the typical building materials where free space propagation and/or reflection are the main mechanisms. To verify this hypothesis, we conducted some measurements in the National Institute of Metrology (NIM) RC (see the Verification in Reverberation Chamber section).

4.3. Path Loss

Figure 7 and "Fit intercept" in Table 2 indicate that the path loss at 14.6 GHz is larger than that at 3.6 GHz. As expected, the higher frequency leads to the larger propagation loss. The "path loss exponent" in Table 2 indicates a minimal difference in the path loss exponent for the two frequency bands. This observation is in line with what was experienced in [8,10,28]. In [8], a multi-frequency (0.8 GHz to 28 GHz) path loss model for external wall attenuation and indoor propagation was presented. For the indoor propagation, the measurement results show that the linear attenuation factor (similar to the path loss exponent) is not very sensitive to the frequency. In [10], the measured path loss exponents are 1.31 and 1.29 for centimeter- and millimeterwave ultra-wideband LOS channels, respectively. In [28], the exponents are similar at 1.33 and 1.31 for 5 and 60 GHz for indoor channels.

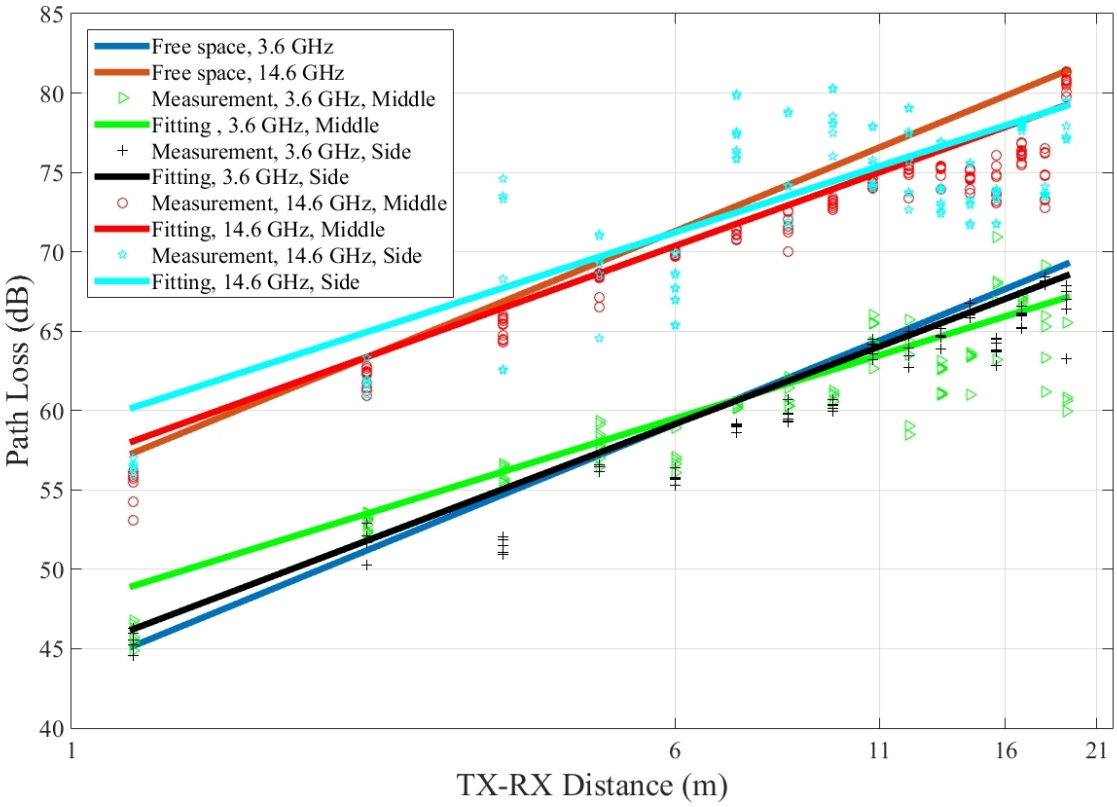

Figure 7. (color online) Path loss versus link distance.

4.4. Coherence Bandwidth

The measurement results in Table 2 indicate that the coherence bandwidths at the two frequency bands are similar. For simplicity, our analysis begins with the two-ray model. The antenna patterns are assumed to be similar for the different frequencies.

For the LOS path, we can express the electric far field at a point u in space as [29]

$$E(f,t) = \frac{\alpha_s(\theta,\psi,f)cos[2\pi f(t-\frac{d}{c})]}{d}, \tag{8}$$

where $\alpha_s(\theta,\psi,f)$ is the radiation pattern of the TX antenna at frequency f in the direction (θ,ψ), d is the distance from the TX to the point u, and the constant c is the speed of light.

Because the phase difference between the two rays determines whether the two waves add constructively or destructively, we focus on the phase of the signal. Then, Equation (8) is simplified as

$$E(f,t) = Acos(2\pi ft+\theta), \tag{9}$$

where A equals $\frac{\alpha_s(\theta,\psi,f)}{d}$, and θ equals $-2\pi f\frac{d}{c}$.

For the reflected path, the electric far field at the point u is expressed as

$$E_r(f,t) = A_r cos[2\pi f(t+\delta t)+\theta], \tag{10}$$

where A_r is the amplitude of the reflected signal, and δt is determined by the distance difference of the two rays. The phase difference between the two rays is

$$\phi = 2\pi f\delta t. \tag{11}$$

For another frequency f', the phase difference is

$$\phi' = 2\pi f' \delta t. \tag{12}$$

The phase difference between the two rays, ϕ, determines the constructive or destructive interference pattern. Then, the difference of ϕ for two frequencies, i.e., $|\phi' - \phi|$, should be insignificant within the coherence bandwidth. The difference of ϕ is

$$|\phi' - \phi| = |2\pi\delta t(f' - f)|. \tag{13}$$

Equation (13) indicates that the coherence bandwidth is related to the relative frequency ($|f' - f|$), not related to the absolute frequency, under the assumption of having similar antenna patterns over the frequency band. Therefore, the coherence bandwidths at 14.6 GHz and 3.6 GHz should be similar. The measurement results verify the above analysis.

5. Verification in Reverberation Chamber

Based on the comparative analysis in Section 4.2, it is hypothesized that the RMS delay spread is independent of the frequency in the scenario where free space propagation and/or reflection are the main mechanisms. We used the RC to verify this hypothesis. The RC provides a reliable, controllable, and repeatable multipath environment where reflection is the main mechanism [30–33].

The RC is essentially an large, electric metal box, having dimensions of 5.09 m × 6.43 m × 5.57 m, as shown in Figure 8. In the RC, reflection is the main propagation mechanism [34]. Inside the chamber, the mechanical stirring was performed by two metal paddles that were moved stepwise. The measurement of RMS delay spread in the RC was repeated for 100 different fixed paddle positions spaced by $360^\circ/100 = 3.6^\circ$. For the RMS delay spread estimation, the 100 measurement results were averaged to obtain the mean values. The RMS delay spread in the chamber can be changed by putting different numbers of RF-absorbing material inside the RC. We repeated the measurements for three and four absorbers, respectively. Each piece of the absorber is with 81 cones in a 9 × 9 array, the cone width is 6.8 cm, and the cone height is 17.8 cm. The transmitting antenna was directed into a corner of the chamber, and the receiving antenna was placed in the middle of the RC.

(a) (b)

Figure 8. NIM (National Institute of Metrology) RC (reverberation chamber). (**a**) appearance of the NIM RC; (**b**) absorbers in the NIM RC.

We measured the channel over the whole frequency range from 3.1 GHz to 15.1 GHz, using the same VNA-based measurement system, as shown in Figure 9. Because the sweep points of the VNA are limited to 60,001, sectional measurement was performed over the whole frequency range. We divided the whole range (3.1 GHz to 15.1 GHz) into 12 frequency bands. For each band, the S_{21} was measured in the 1 GHz bandwidth with 60,001 sweep points.

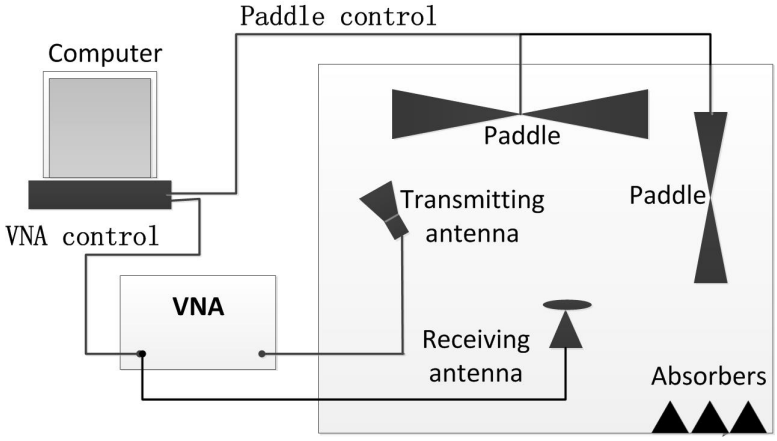

Figure 9. RMS (root-mean-square) delay spread measurement setup in the NIM RC.

Figure 10a shows the measurement results and the linear fitting lines. The slopes of these fitting lines are −0.0020 ns/MHz and −0.0026 ns/MHz for the 3 and 4 absorbers, respectively. It is confirmed that the difference is minimal in the RMS delay spread for the whole sweep frequency range. In order to analyze the behavior of the RMS delay spread for a given frequency band with higher frequency resolution, we use a 200 MHz bandpass filter in postprocessing. This filter is applied to the measured S_{21} frequency-domain data, and the RMS delay spread is calculated for different filter center frequencies. As shown in Figure 10b, the slopes of the fitting lines are −0.0023 ns/MHz and −0.0032 ns/MHz for the 3 and 4 absorbers, respectively.

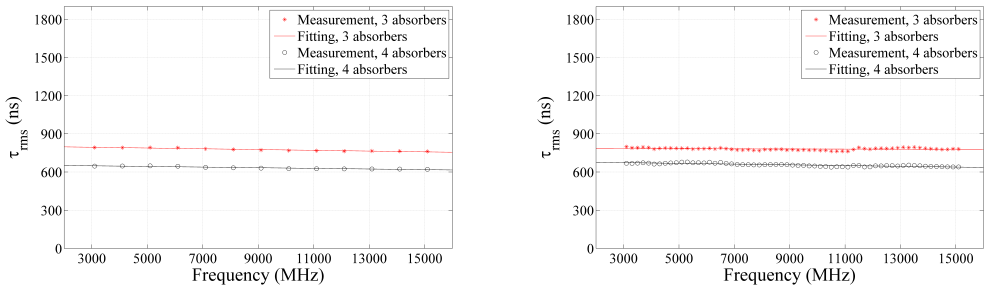

Figure 10. (color online) RMS delay spread in the NIM RC calculated over (**a**) 1000 MHz bandwidth; and (**b**) 200 MHz bandwidth.

The coherence bandwidths in the RC are calculated via Equation (3) based on the measurement data. It is shown in Figure 11 that the coherence bandwidth is also similar in the frequency range. The slopes for the RMS delay spread and coherence bandwidth are summarized in Table 3. The measurement results imply that the RMS delay spread and coherence bandwidth are not sensitive to the frequency in the RC.

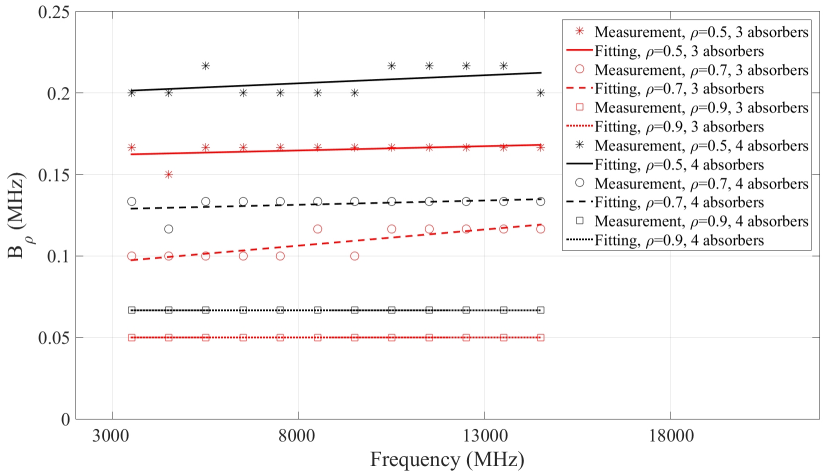

Figure 11. (color online) Coherence bandwidth in the NIM RC calculated over a 1 GHz bandwidth as a function of center frequency.

Table 3. Slopes for RMS (root-mean-square) delay spread and coherence bandwidth in the NIM (National Institute of Metrology) RC (reverberation chamber).

Measured Parameters	Slope	
	3 Absorbers	4 Absorbers
RMS delay spread, 1000 MHz (ns/MHz)	-0.20×10^{-3}	-0.21×10^{-3}
RMS delay spread, 200 MHz (ns/MHz)	-0.23×10^{-3}	-0.32×10^{-3}
Coherence bandwidth, ρ = 0.5	5.24×10^{-6}	9.91×10^{-7}
Coherence bandwidth, ρ = 0.7	1.98×10^{-6}	5.25×10^{-7}
Coherence bandwidth, ρ = 0.9	1.92×10^{-21}	4.46×10^{-21}

6. Conclusions

Based on measurements, we presented an analysis of indoor channels for the corridor scenario at 3.6 GHz and 14.6 GHz frequency bands with the directional antennas. From the comparative analysis for the corridor, we show that the path loss is larger at 14.6 GHz frequency. The difference of the path loss exponents in the two frequency bands is less than 0.18 in the corridor. The main reason is that the path loss exponent is relevant to the relative power in the distance domain. For the RMS delay spread and coherence bandwidth, they are relevant to the relative power in the time domain. The constant reflection coefficient makes them not very sensitive to the frequency in the corridor. The differences between the two frequency bands are less than 1 ns and 6 MHz for RMS delay spread and coherence bandwidth, respectively. Based on the comparative analysis, it is hypothesized that the RMS delay spread and coherence bandwidth are independent of frequency in the typical indoor scenarios where free space propagation and/or reflection are the main mechanisms. The measurement results in the highly reflective environment (RC) and common reflective environment (corridor) verify the hypothesis.

This analysis helps readers to understand the essence of the propagation. Both the quantitative results and qualitative analysis are useful for the needed extensions/modifications of channel modeling from the low frequency band to the high frequency band.

Acknowledgments: The authors would like to thank Andreas Molisch for valuable guidance with regard to the antenna influence on channel characteristics. The authors also thank Donglin Meng and Xiao Liu for their assistance during the revision stage. This work was supported in part by the National Natural Science Foundation of China under Grant 61501020 and 61501021, by the State Key Laboratory of Rail Traffic Control and Safety under Grant RCS2016ZJ005 and RCS2016ZJ004, by the National Key Technology R&D Program under

Grant 2014BAK02B05, by the Fundamental Research Funds for the Central Universities under Grants 2016JBZ006 and 2016JBM075, by the Fundamental Funds of National Institute of Metrology under Grant 27-AKY1507 and 27-ANL604, and by the China Postdoctoral Science Foundation under Grant 2016M591355.

Author Contributions: Xin Zhou, Zhangdui Zhong and Xin Bian conceived and designed the experiments; Xin Zhou, Ruisi He and Xiaotao Guo performed the experiments; Xin Zhou, Ruoyu Sun, Ke Guan and Ke Liu analyzed the data; all authors wrote the paper.

Conflicts of Interest: The authors declare no conflict of interest.

References

1. Osseiran, A.; Boccardi, F.; Braun, V.; Kusume, K.; Marsch, P.; Maternia, M.; Queseth, O.; Schellmann, M.; Schotten, H.; Taoka, H.; et al. Scenarios for 5G mobile and wireless communications: The vision of the metis project. *IEEE Commun. Mag.* **2014**, *52*, 26–35.
2. Medbo, J.; Borner, K.; Haneda, K.; Hovinen, V.; Imai, T.; Jarvelainen, J.; Jamsa, T.; Karttunen, A.; Kusume, K.; Kyrolainen, J.; et al. Channel modelling for the fifth generation mobile communications. In Proceedings of the 2014 8th European Conference on Antennas and Propagation, The Hague, The Netherlands, 6–11 April 2014; pp. 219–223.
3. Wang, Y.; Li, J.; Huang, L.; Jing, Y.; Georgakopoulos, A.; Demestichas, P. 5G mobile: Spectrum broadening to higher-frequency bands to support high data rates. *IEEE Veh. Technol. Mag.* **2014**, *9*, 39–46.
4. Gozalvez, J. 5G tests and demonstrations [mobile radio]. *IEEE Veh. Technol. Mag.* **2015**, *10*, 16–25.
5. He, R.; Zhong, Z.; Ai, B.; Ding, J. An empirical path loss model and fading analysis for high-speed railway viaduct scenarios. *IEEE Antennas Wirel. Propag. Lett.* **2011**, *10*, 808–812.
6. He, R.; Zhong, Z.; Ai, B.; Wang, G.; Ding, J.; Molisch, A.F. Measurements and analysis of propagation channels in high-speed railway viaducts. *IEEE Trans. Wirel. Commun.* **2013**, *12*, 794–805.
7. He, R.; Ai, B.; Wang, G.; Guan, K.; Zhong, Z.; Molisch, A.F.; Briso-Rodriguez, C.; Oestges, C.P. High-speed railway communications: From GSM-R to LTE-R. *IEEE Veh. Technol. Mag.* **2016**, *11*, 49–58.
8. Rodriguez, I.; Nguyen, H.; Sorensen, T.; Kovacs, I.; Mogensen, P. An empirical outdoor-to-indoor path loss model from below 6 GHz to cm-wave frequency bands. *IEEE Antennas Wirel. Propag. Lett.* **2016**, *PP*, doi:10.1109/LAWP.2016.2633787.
9. Davies, R.; Bensebti, M.; Beach, M.A.; McGeehan, J.P. Wireless propagation measurements in indoor multipath environments at 1.7 GHz and 60 GHz for small cell systems. In Proceedings of the 41st IEEE Vehicular Technology Conference, St. Louis, MO, USA, 19–22 May 1991; pp. 589–593.
10. Martinez-Ingles, M.T.; Molina-Garcia-Pardo, J.M.; Rodriguez, J.V.; Pascual-Garcia, J.; Juan-Llacerj, L.; Experimental comparison between centimeter- and millimeter-wave ultrawideband radio channels. *Radio Sci.* **2014**, *49*, 450–458.
11. Nie, S.; Maccartney, G.R.; Sun, S.; Rappaport, T.S. 72 GHz millimeter wave indoor measurements for wireless and backhaul communications. In Proceedings of the 2013 IEEE 24th International Symposium on Personal Indoor and Mobile Radio Communications (PIMRC), London, UK, 8–11 September 2013; pp. 2429–2433.
12. Siamarou, A.G.; Al-Nuaimi, M. A wideband frequency-domain channel-sounding system and delay-spread measurements at the license-free 57- to 64-GHz band. *IEEE Trans. Instrum. Meas.* **2010**, *59*, 519–526.
13. Hammoudeh, A.; Scammell, D.A. Sanchez, M.G. Measurements and analysis of the indoor wideband millimeter wave wireless radio channel and frequency diversity characterization. *IEEE Trans. Antennas Propag.* **2003**, *51*, 2974–2986.
14. Remley, K.A.; Young, W.F.; Healy, J. *Analysis of Radio-Propagation Environments to Support Standards Development for RF-Based Electronic Safety Equipment*; US Department of Commerce, National Institute of Standards and Technology: Boulder, CO, USA, 2012.
15. Sun, R.; Matolak, D.W. Characterization of the 5-GHz elevator shaft channel. *IEEE Trans. Wirel. Commun.* **2013**, *12*, 5138–5145.
16. Ping, C.; Lim, E. Computational Electromagnetic Modeling for Wireless Channel Characterization. Ph.D. Thesis, Ohio State University, Columbus, OH, USA, September 2006.
17. ITU-R. *Multipath Propagation and Parameterization of Its Characteristics*; International Telecommunication Union: Geneva, Switzerland, 2003.

18. Molisch, A.F.; Steinbauer, M. Condensed parameters for characterizing wideband mobile radio channels. *Int. J. Wirel. Inf. Netw.* **1999**, *6*, 133–154.
19. Molisch, A.F. *Wireless Communications*; John Wiley and Sons: New York, NY, USA, 2005.
20. Kivinen, J.; Zhao, X.; Vainikainen, P. Empirical characterization of wideband indoor radio channel at 5.3 GHz. *IEEE Trans. Antennas Propag.* **2001**, *49*, 1192–1203.
21. Akl, R.; Tummala, D.; Li, X. Indoor propagation modeling at 2.4 GHz for IEEE 802.11 networks. In Proceedings of the Sixth IASTED International Multi-Conference on Wireless and Optical Communications, Banff, AB, Canada, 3–5 July 2006.
22. Geng, S.; Kivinen, J.; Zhao, X.; Vainikainen, P. Millimeter-wave propagation channel characterization for short-range wireless communications. *IEEE Trans. Veh. Technol.* **2009**, *28*, 3–13.
23. He, R.; Chen, W.; Ai, B.; Molisch, A.F.; Wang, W.; Zhong, Z.; Yu, J.; Sangodoyin, S. On the clustering of radio channel impulse responses using sparsity-based methods. *IEEE Trans. Antennas Propag.* **2016**, *64*, 2465–2474.
24. Rappaport, T. *Wireless Communications: Principles and Practice*; Prentice Hall: New York, NY, USA, 2001.
25. Salous, S. *Radio Propagation Measurement and Channel Modelling*; John Wiley and Sons: New York, NY, USA, 2012.
26. Huang, F.; Tian, L.; Zheng, Y.; Zhang, J. Propagation characteristics of indoor radio channel from 3.5 GHz to 28 GHz. In Proceedings of the IEEE Vehicular Technology Conference, Montreal, QC, Canada, 18 September 2016.
27. Janssen, G.J.M.; Stigter, P.A.; Prasad, R. Wideband indoor channel measurements and BER analysis of frequency selective multipath channels at 2.4, 4.75, and 11.5 GHz. *IEEE Trans. Commun.* **1996**, *44*, 1272–1288.
28. Peter, M.; Keusgen, W. Analysis and comparison of indoor wideband radio channels at 5 and 60 GHz. In Proceedings of the European Conference on Antennas and Propagation, Berlin, Germany, 23–27 March 2009; pp. 3830–3834.
29. Tse, D.; Viswanath, P.; *Fundamentals of Wireless Communication*; Cambridge University Press: Cambridge, UK, 2005.
30. Holloway, C.L.; Hill, D.A.; Ladbury, J.M.; Wilson, P.F. On the use of reverberation chambers to simulate a Rician radio environment for the testing of wireless devices. *IEEE Trans. Antennas Propag.* **2006**, *54*, 3167–3177.
31. Micheli, D.; Barazzetta, M.; Carlini, C.; Diamanti, R.; Mariani Primiani, V.; Moglie, F. Testing of the carrier aggregation mode for a live LTE base station in reverberation chamber. *IEEE Trans. Veh. Technol.* **2016**, *PP*, doi:10.1109/TVT.2016.2587662.
32. Santoni, F.; Pastore, R.; Gradoni, G.; Piergentili, F.; Micheli, D.; Diana, R.; Delfini, A. Experimental characterization of building material absorption at mmwave frequencies: By using reverberation chamber in the frequency range 50–68 GHz. In Proceedings of the 2016 IEEE Metrology for Aerospace (MetroAeroSpace), Florence, Italy, 22–23 June 2016; pp. 166–171.
33. Gagliardi, L.; Micheli, D.; Gradoni, G.; Moglie, F.; Primiani, V.M. Coupling between multipath environments through a large aperture. *IEEE Antennas Wirel. Propag. Lett.* **2015**, *14*, 1463–1466.
34. Genender, E.; Holloway, C.L.; Remley, K.A.; Ladbury, J.M.; Koepke, G.; Garbe, H. Simulating the multipath channel with a reverberation chamber: Application to bit error rate measurements. *IEEE Trans. Electromagn. Compat.* **2010**, *52*, 766–777.